10-21-2009

A Counterpart to the Radial-Orbit Instability in Triaxial Stellar Systems

Fabio Antonini
Rochester Institute of Technology

Roberto Capuzzo-Dolcetta
University of Rome

David Merritt
Rochester Institute of Technology

Recommended Citation

F. Antonini, R. Capuzzo-Dolcetta, D. Merritt; A counterpart to the radial-orbit instability in triaxial stellar systems, Monthly Notices of the Royal Astronomical Society, Volume 399, Issue 2, 21 October 2009, Pages 671–682, https://doi.org/10.1111/j.1365-2966.2009.15342.x

Draft version January 28, 2009
Preprint typeset using LaTeX style emulateapj v. 10/09/06

A COUNTERPART TO THE RADIAL-ORBIT INSTABILITY IN TRIAXIAL STELLAR SYSTEMS

Fabio Antonini
Department of Physics, University of Rome 'La Sapienza', P.le A. Moro 5, I-00185, Rome, Italy, and Dept. of Physics, Rochester Institute of Technology, 85 Lomb Memorial Drive, Rochester, NY 14623, USA

Roberto Capuzzo-Dolcetta
Department of Physics, University of Rome 'La Sapienza', P.le A. Moro 5, I-00185, Rome, Italy

David Merritt
Department of Physics and Center for Computational Relativity and Gravitation, Rochester Institute of Technology, 85 Lomb Memorial Drive, Rochester, NY 14623, USA
Draft version January 28, 2009

ABSTRACT

Self-consistent solutions for triaxial mass models are highly non-unique. In general, some of these solutions might be dynamically unstable, making them inappropriate as descriptions of steady-state galaxies. Here we demonstrate for the first time the existence in triaxial galaxy models of an instability similar to the radial-orbit instability of spherical models. The instability manifests itself when the number of box orbits, with predominantly radially motions, is sufficiently large. N-body simulations verify that the evolution is due neither to chaotic orbits nor to departures of the model from self-consistency, but rather to a collective mode. The instability transforms the triaxial model into a more prolate, but still triaxial, configuration. Stable triaxial models are obtained when the mass contribution of radial orbits is reduced. The implications of our results for the shapes of dark-matter halos are discussed.

Subject headings: galaxies: elliptical and lenticular, cD - stellar dynamics - methods:numerical, (cosmology:) dark matter

1. INTRODUCTION

Even in a collisionless stellar system, it is possible for density perturbations to grow, by inducing motions that reinforce the original overdensity. Such collective instabilities typically require the unperturbed motion to be highly correlated, and they have been most thoroughly studied in thin disks, which are subject to a variety of instabilities when sufficiently "cold." In elliptical galaxies, where the stellar motions are more nearly random in direction, density perturbations might be expected to rapidly attenuate as the stars move along their respective orbits. However it turns out that the motion in a variety of physically reasonable models of "hot" stellar systems is sufficiently correlated to induce growing modes (as reviewed by Merritt 1999). The two classes of instability that have most thoroughly been studied in this context are bending instabilities, which are driven by the centrifugal force of stars moving across a bend (Toomre 1966); and the radial-orbit instability (henceforth ROI), which is caused by the tendency of eccentric orbits to clump around a bar-like distortion (Antonov 1973; Lynden-Bell 1979). Bending instabilities may be responsible for the lack of elliptical galaxies more elongated than $\sim 1:3$ (Polyachenko & Shukhman 1977; Merritt & Sellwood 1994); simulated dark-matter halos also appear never to exceed this degree of elongation, presumably because more flattened halos "puff up" due to the instability (e.g. Bett et al. 2007). The ROI, on the other hand, can be present even in precisely spherical galaxies if they contain an abundance of stars on elongated orbits. It manifests itself most naturally in collapse simulations, which produce prolate/triaxial bars if the initial conditions are sufficiently cold (Merritt & Aguilar 1985). The ROI has also been invoked as a factor that regulates the density profiles of simulated dark-matter halos (Bellovary et al. 2008).

Construction of stationary models of hot stellar systems can be difficult, and this is one reason why most of the studies cited above have adopted highly symmetric models: typically spherical, in the case of the ROI, and axisymmetric in the case of the bending mode studies. But there is no reason why such instabilities should be limited to spherical or axisymmetric models. Here, we report on a dynamical instability in triaxial models that closely mimics in its behavior the ROI of spherical models. As in the spherical case, the instability leads to a final configuration that is close to prolate. Our simulations provide the first concrete evidence that dynamical instabilities may limit the permitted range of shapes of triaxial stellar systems, a result that may have implications for our understanding of elliptical galaxy and dark halo dynamics.

The self-consistent triaxial models on which our work is based were described in an earlier paper (Capuzzo-Dolcetta et al. 2007). We briefly describe these models in §2. The discretized models are described in §3, and the results of N-body integrations in §4 and §5. §6 explores the dependence of the stability properties of the models on their orbital composition. §7 discusses the implications for the dynamics of elliptical galaxies

Electronic address: antonini@astro.rit.edu
Electronic address: roberto.capuzzodolcetta@uniroma1.it
Electronic address: merritt@astro.rit.edu

and dark matter halos. §8 sums up.

2. THE SELF-CONSISTENT TRIAXIAL MODELS

The instability was discovered while testing, by N-body simulations, the equilibrium characteristics of the triaxial galaxy models constructed in CLMV07. In this section we summarize the way in which the self-consistent orbital solutions were obtained and in the next section we discuss the discretized models used in the N-body simulations.

CLMV07 constructed three different self-consistent solutions of triaxial, cuspy elliptical galaxies embedded in triaxial dark halos. The systems differ in terms of the shape of the dark matter halo: (i) one halo has the same axis ratios as the luminous matter (1:0.86:0.7); (ii) the second halo has a more prolate shape (1:0.66:0.5); (iii) the third halo has a more oblate shape (1:0.93:0.7). Our choice was to study the dynamical features of the most interesting case of maximal triaxiality (i.e., the model with triaxiality parameter $T \equiv (a^2-b^2)/(a^2-c^2) = 1/2$), and to study the time evolution of the two self-consistent solutions (MOD1 and MOD1-bis) obtained in CLMV07 for this case. The main difference between these two solutions was the maximum time adopted for the orbital integrations, which was, in MOD1-bis, longer (~ 5 Hubble times) than in MOD1 (~ 2 Hubble times). The models were constructed by means of the orbital superposition method introduced by Schwarzschild (1979) which relies on an optimization technique. The optimization problem consisted in minimizing the discrepancy between the model cell masses obtained by integration of the given analytical density law $\rho(x,y,z)$ and those given by a linear combination of the orbits computed in the potential generated by ρ. In our case, the two quantities to be independently minimized were

$$\chi^2_{lm} = \frac{1}{N_{cells}} \sum_{j=1}^{N_{cells}} \left(M_{j;lm} - \sum_{k=1}^{n_{orb}} C_{k;lm} B_{k,j;lm} \right)^2 , \quad (1)$$

$$\chi^2_{dm} = \frac{1}{N_{cells}} \sum_{j=1}^{N_{cells}} \left(M_{j;dm} - \sum_{k=1}^{n_{orb}} C_{k;dm} B_{k,j;dm} \right)^2 , \quad (2)$$

where $B_{k;j;lm(dm)}$ is the fraction of time that the kth orbit spends in the jth cell of the luminous-matter grid (dark-matter grid); $M_{j;lm(dm)}$ is the mass which the model places in the jth cell of the luminous-matter grid (dark-matter grid). $C_{k;lm}$ and $C_{k;dm}$ represent the total mass, respectively, of the luminous and dark matter component assigned to the kth orbit ($1 \le k \le n_{orb}$). The basic constraints were $C_{k;lm} \ge 0$ and $C_{k;dm} \ge 0$, i.e., non-negative orbital weights. The departure from self-consistency was measured in CLMV07 by

$$\delta = \frac{\sqrt{\chi^2}}{\overline{M}} \quad , \quad (3)$$

where $\overline{M}$ is the average mass contained in the grid cells and χ^2 are the quantities defined above; thus δ represents the fractional rms deviation in the cell masses.

The mass model considered in CLMV07 for the luminous component was a triaxial generalization of Dehnen's (1993) spherical model with a "weak" inner cusp, $\rho \sim r^{-1}$. The luminous mass density was

$$\rho_l(m) = \frac{M_l}{2\pi a_l b_l c_l} \frac{1}{m(1+m)^3} \quad (4)$$

$$m^2 = \frac{x^2}{a_l^2} + \frac{y^2}{b_l^2} + \frac{z^2}{c_l^2}, \qquad 0 < c_l < b_l < a_l \quad (5)$$

and M_l the total luminous mass. For the dark component the adopted mass density was

$$\rho_{dm}(m') = \frac{\rho_{dm,0}}{(1+m')(1+m'^2)} \quad (6)$$

$$m'^2 = \frac{x^2}{a_{dm}^2} + \frac{y^2}{b_{dm}^2} + \frac{z^2}{a_{dm}^2} \quad (7)$$

and $\rho_{dm,0}$ the central dark matter density (Burkert 1995). Therefore the dark component has a low-density core.

In the present work we adopt the same units used in CLMV07: $G = a_l = M_l = 1$. Consequently, the time unit is:

$$[T] = G^{-1/2} {a_l}^{3/2} {M_l}^{-1/2} \quad (8)$$

$$= 1.49 \times 10^6 \mathrm{yr} \Big(\frac{M_l}{10^{11} M_\odot} \Big)^{-1/2} \Big(\frac{a_l}{1\mathrm{kpc}} \Big)^{3/2} . \quad (9)$$

The, derived, velocity and energy units are $V_u = \sqrt{G M_l / a_l}$ and $E_u = (G {M_l}^2 / a_l)$, respectively. In this units the half mass crossing time of the system is:

$$t_{cross} = \left(\frac{G\,(M_l + M_d)}{{r_h}^3} \right)^{-1/2} = 17.78\,[T] \quad (10)$$

where r_h is the radius containing half of the model mass, considering the dark matter halo truncated at $r = 80$; M_d is the total mass of the dark matter component. In the following, this time will be considered the reference time scale.

3. DISCRETIZED MODELS AND THEIR PROPERTIES

In this section we explain the methods we used to discretize the self-consistent models described above and how we computed their properties for the N-body simulations. We also present some kinematical features of the models that are relevant to their stability properties.

3.1. *Discretization*

The initial conditions for the N-body integrations were set by populating the generic kth orbit with a number of particles proportional to C_k and randomly choosing positions and velocities from the recorded data of the orbital integrations. In more detail:

1 The values C_k for both the dark matter and the luminous matter are read from model data and the following quantities are evaluated:

$$N_{k;lm} = C_{k;lm} / m_{lm} \quad , \quad (11)$$

$$N_{k,dm} = C_{k;dm} / m_{dm} \quad , \quad (12)$$

$$N_k = N_{k;lm} + N_{k;dm} \quad , \quad (13)$$

where N_k is the total number of particles that populate the kth orbit while $N_{k;lm}$, $N_{k;dm}$ are the number of stars and dark matter particles, respectively; m_{dm} and m_{lm} are free parameters that specify the mass of individual star and dark matter particles.

2 $N_{k,dm}$ particles with masses m_{dm}, and $N_{k,lm}$ particles with masses m_{lm}, are selected with positions and velocities drawn uniformly and randomly (with respect to time) from the stored positions and velocities of the orbit integration.

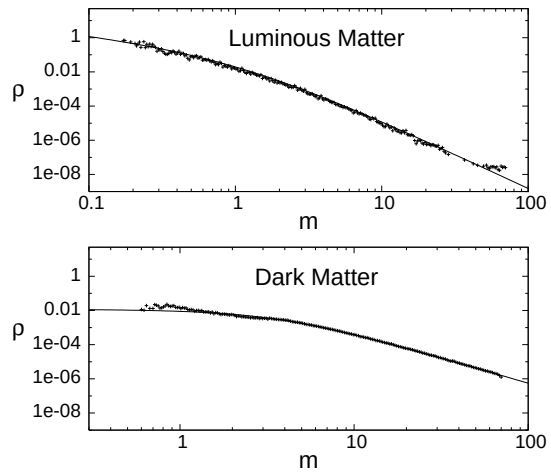

FIG. 1.— Density profiles of the discretized model MOD1-bis plotted versus elliptical radius m; the curves are the analytic input profiles.

3 If N_k is greater than the number of available data in "initial data", further positions and velocities are assigned using a cubic spline interpolant.

These steps are repeated for all orbits of the self-consistent model. In this way the mass distributions of the models are adequately reproduced as long as the various orbits are populated with a sufficiently large number of particles.

The total number of objects depends on m_{dm} and m_{lm} as

$$N_{dm} = \frac{1}{m_{dm}} \sum_{k=1}^{n_{dorb}} C_{k;dm}, \tag{14}$$

$$N_{lm} = \frac{1}{m_{lm}} \sum_{k=1}^{n_{lorb}} C_{k;lm}. \tag{15}$$

We chose to assign the same mass to each particle of the same type (luminous or dark matter), hence different numbers of particles are spread on orbits with different values of C_k. However, different values were chosen for the mass associated with dark and luminous components. We took $m_l = 5 \times 10^{-5}$ and $m_{dm} = 7 \times 10^{-5}$ which gave, for instance in the case of MOD1-bis, a total of 166194 particles, of which 19709 were "stars" and 146485 "dark matter"; the mean number of particles per orbit was 36. With this resolution the theoretical mass profiles were well reproduced as shown in Figures 1 and 2 for model MOD1-bis.

3.2. *Determination of shapes*

The evolution of the shape of the N-body systems was studied by computing the axis ratios at different distances from the center, and also by constructing isodensity contours.

The symmetry axes were determined from the inertia tensor as

$$\zeta = \sqrt{T_{11}/T_{max}}\ , \quad \eta = \sqrt{T_{22}/T_{max}}\ , \quad \theta = \sqrt{T_{33}/T_{max}} \tag{16}$$

where T_{ii} are the principal moments of the inertia tensor and $T_{max} = \max\{T_{11}, T_{22}, T_{33}\}$. Referring to a coordinate system in which the inertia tensor is diagonal, the assumption $\zeta = 1$ (i.e., $T_{11} = T_{max}$) implies

$$\eta = \sqrt{\frac{\sum m_i y_i^2}{\sum m_i x_i^2}}, \quad \theta = \sqrt{\frac{\sum m_i z_i^2}{\sum m_i x_i^2}}\ . \tag{17}$$

The axis ratios of the models were computed through the standard procedure described by Katz (1991) (similar methods are described by Dubinski & Carlberg (1991) and Poon & Merritt (2004)). To evaluate the system shape within a sphere of radius d, the following iterative method was used:

1. The inertia tensor defined by particles within a sphere of radius d is calculated.

2. The axis ratios are determined from equation (16).

3. New axis ratios are computed considering only particles enclosed in the ellipsoidal volume having the axis ratios determined in step 2. Therefore, a particle i is included in the summations if $q_i < d$, where

$$q_i^2 = \left(\frac{x_i}{\zeta}\right)^2 + \left(\frac{y_i}{\eta}\right)^2 + \left(\frac{z_i}{\theta}\right)^2. \tag{18}$$

These three steps are iterated until the axis ratios converge. Finally, we defined $a > b > c$ assuming $c/a = \min\{\zeta, \eta, \theta\}$ and b/a the intermediate value between (ζ, η, θ). Evaluation of the axis ratios of the discretized models verified the accuracy of the technique: for the solution MOD1-bis we found $b/a = 0.86$, $c/a = 0.69$ for the luminous matter at $r = 12$ and $b/a = 0.86$, $c/a = 0.72$ for the dark matter at $r = 25$, compared with the given values $b/a = 0.86$, $c/a = 0.70$ of the analytical density law.

3.3. *Specification of streaming motions*

$X(Z)$-tube orbits are here defined as those orbits having a non-vanishing $x(z)$ component of the time-averaged angular momentum; all other, non-tube orbits (either box or chaotic) are defined as *semi-radial orbits*. Figure 3 shows the cumulative energy distributions of the various orbital families in the discretized models. There are significant contributions from both tube and semi-radial orbits in both the luminous and dark components.

A choice must be made concerning the sense of rotation of particles placed initially on tube orbits (Schwarzschild 1979; Merritt 1980). The time-averaged density of an orbit is invariant to a change in sign of the initial velocity; maximum rotation (i.e. streaming) is obtained if all particles on each tube orbit have the same sense of rotation, while zero mean motion is achieved by populating the tube orbits equally in both directions. To investigate the effects of non-zero streaming, we constructed two discretizations of each self-consistent solution having the two extreme cases of maximum and minimum net streaming. In Table 1 some parameters of four N-body systems, sampling MOD1 and MOD1-bis, are given.

3.4. *Model kinematics*

The kinematical features of the discretized models were analyzed by computing the first and the second moments of the stellar distribution function on a spatial grid (e.g. Merritt 1980).

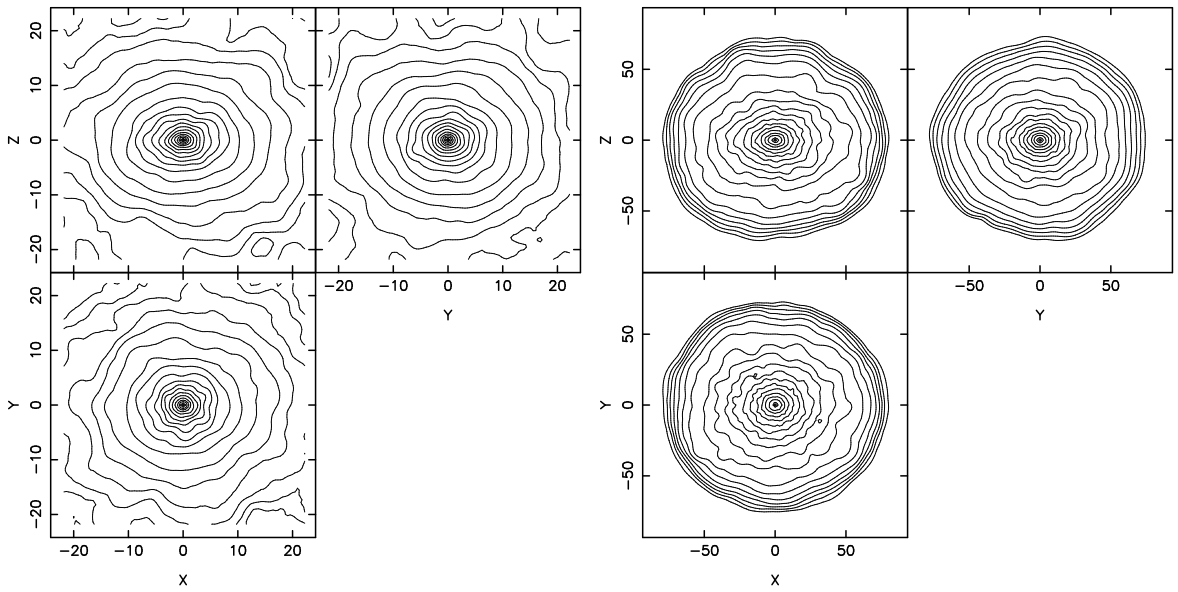

FIG. 2.— Contours of the projected density for the N-body initial conditions illustrated in Figure 1 for the luminous matter (left) and the dark matter (right).

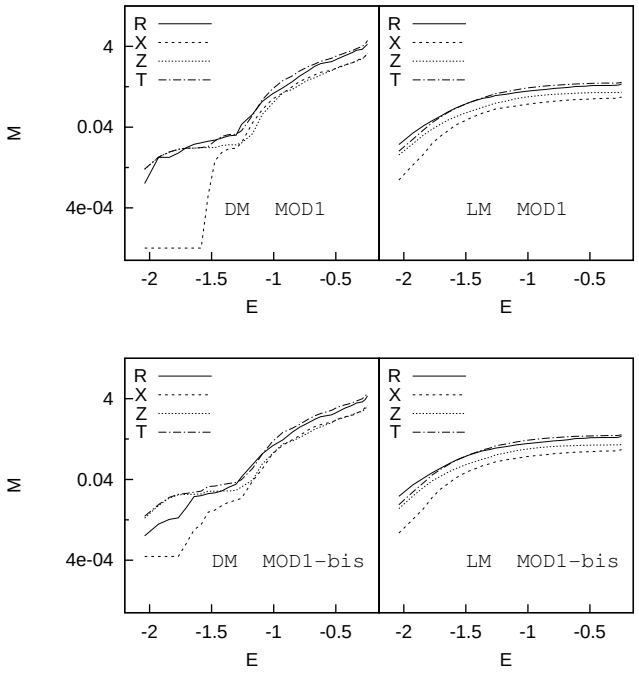

FIG. 3.— Cumulative (by mass) energy distributions of the various orbital families for the dark matter (DM) and the luminous component (LM), in the self-consistent solutions $MOD1$ (top) and $MOD1-bis$ (bottom). The symbols "R", "X", "Z" and "T" denote the mass contributed by semi-radial, X-tube, Z-tube and tube orbits, respectively.

We used different, Cartesian grids for the two different matter components. In the case of the *dark matter grid* the cells were cubes with sides of length 6 and all cells had the same size. Because of the high density concentration of the luminous component, we used grid cells with a range of sizes for the *luminous matter grid*. This grid consisted of a set of cubic cells with sizes ranging from 0.5 near the center to 2 at greater distances.

TABLE 1
FEATURES OF N-BODY MODELS.

System	*Solution*	L	N_{lm}	N_{dm}
HL	$MOD1$	23.71448	19684	144886
HL_{bis}	$MOD1-bis$	23.57945	19709	146485
LL	$MOD1$	0.401937	19684	144886
LL_{bis}	$MOD1-bis$	0.337428	19709	146485

NOTE. — The acronyms HL and LL stand for "high L" and "low L" where L is the absolute value of the angular momentum.

A total of nine quantities were averaged for both matter components in each cell: the mean velocity $\langle V_i \rangle$ and the six independent components of the tensor $\langle V_i V_j \rangle$. In this way the velocity dispersion tensor,

$$\sigma_{ij}^2 \equiv \langle V_i V_j \rangle - \langle V_i \rangle \langle V_j \rangle,$$

could be evaluated in each cell. Then, σ_{ij}^2 was diagonalized obtaining the three "principal" dispersions, and the three direction cosines giving the directions of the eigenvectors.

Figure 4 shows the velocity anisotropy in the $x-y$ plane for MOD1-bis in the case of high angular momentum. The length of each cross arm is proportional to the principal value of σ_{ij}^2. Some important features are: (1) a high degree of anisotropy in both components at all radii; (2) a nearly constant (as a function of radius) radial velocity dispersion of the luminous matter. On the other side, the radial velocity dispersion of the dark matter decreases strongly with radius.

We evaluated the "anisotropy parameter" $2T_r/T_t$ where $T_r = \langle v_r^2/2 \rangle$ and $T_t = \langle v_t^2/2 \rangle$ (in full isotropy, $2T_r/T_t = 1$). We stress that the interpretation of this parameter, which is straightforward in spherical geometry, is more complicated in the triaxial case. Nevertheless, they give some indication of the average degree of velocity anisotropy. All of our discretized models yielded about the same values for the anisotropy parameters: $(2T_r/T_t)_{dm} \sim 2$ and $(2T_r/T_t)_{lm} \sim 1.4$. The high degree of "anisotropy" in the dark component – too large to be accounted for simply in terms of the triaxial ge-

ometry – suggests a strong bias toward radial motions in the dark matter halo, as indeed can be seen in Figure 4.

4. FIXED-POTENTIAL INTEGRATIONS

Following Smith & Miller (1982), a useful technique for checking whether a discrete, N-body representation of an equilibrium model was correctly constructed is to integrate the discretized initial conditions in the *fixed* potential of the analytic model and observe whether there is any change in the spatial distribution of the N particles. This procedure is also a powerful way to constrain the nature of any evolution that is observed in the full N-body integrations. Actually, if the shape of a model changes with time, this could be due either to chaotic evolution of individual orbits (mixing), or to collective modes (dynamical instability). But the former mechanism will be active even when the potential is fixed, whereas a collective mode requires an evolving potential.

Accordingly, we integrated the orbits of the discretized models in the analytic potential corresponding to the smooth mass distributions (equations 2,2). Each particle was advanced, up to 30 crossing times, using a 7/8 order Runge-Kutta algorithm described by Fehlberg (1968) with a variable time step, in order to keep the relative error per step in energy less than a specified value (10^{-8}). Since each orbit is independent, this operation is easily parallelized. The simulation required $\sim$ 5 CPU hours total for 166000 particles. Registration of the particle positions and velocities were made at fixed intervals of time, the same for all particles. The duration of $30t_{cross}$ is longer than the time over which the instability manifests itself in the full N-body simulations (see below).

Figure 5 shows that no significant evolution of the axis ratios is observed in the fixed potential integrations. Also the contours of the projected density for both systems remain approximately unchanged until the end of the integrations. Actually, the relative variations of the axis ratios with respect to their initial values are within 4% for the luminous component and 1% for the dark matter. Given the unavoidable noise in the computation of the axis ratios, such variations are irrelevant; the larger variations in the luminous matter are probably a consequence of the higher noise due the lower number of particles. These results allow us to conclude that the initial conditions were correctly generated, and also that any strong global shape deformations in the full N-body simulations must be a manifestation

of a dynamical instability, and not chaotic mixing of individual orbits.

5. N-BODY INTEGRATIONS

5.1. *N-Body code*

The full N-body integrations were carried out using the `TreeATD` code of Miocchi & Capuzzo-Dolcetta (2002), which is a parallel code that uses a tree algorithm for the gravitational force evaluation, and an individual time stepping for the leap-frog integrator. `TreeATD` needs three input parameters that influence the speed and accuracy of a simulation: the opening angle θ, the smoothing length ϵ, and the maximum allowed time step Δt. We set $\epsilon = 0.05$ and $\epsilon = 0.1$ in the case of model LL_{bis}, $\Delta t = 0.07$ and $\theta = 0.7$. These values were chosen in order to conserve energy within 0.05% over the full course of the integrations. Simulations were performed using 8 nodes of `gravitySimulator`, a 32-node cluster at the Rochester Institute of Technology.

5.2. *The instability*

The N-body integrations revealed that both MOD1 and MOD1-bis represent unstable equilibria, in the sense that their axis ratios evolve significantly. Lagrangian radii for both models showed essentially no evolution, indicating that the instability affects only the shapes of the models and not the global concentration of matter.

Figure 6 illustrates the change of the axis ratios up to $t = 711.2$ (40 crossing times) for the maximum-streaming models HL and HL_{bis}. Strong deformations appear evidently in both the luminous and dark components after just two crossing times. The initial evolution is toward a more spherical shape; the duration of this first phase is different in the two components, being longer for the dark component than for the luminous component. Final shapes are nearly prolate, with $0.7 < b/a < 0.77$ and $0.65 < c/a < 0.7$ for the dark halo and $0.69 < b/a < 0.71$ and $0.59 < c/a < 0.62$ for the luminous matter. The final contours of the projected density for model HL are shown in Figure 7. After $\sim$ 25 crossing times (dark matter) and 18 crossing times (luminous matter), the instability appears to have run its course, but the system still exhibits a slow figure rotation, as shown in Figure 8.

In order to understand better the influence of model rotation on the dynamical evolution, we performed a second set of simulations for the systems LL and LL_{bis}, which correspond to the case of minimum angular momentum. The right columns of Figure 6 display the evolution of the axis ratios for models LL and LL_{bis}, while Figure 9 shows the contours of the projected density for both the mass components at the final time for model LL. The results confirm that figure rotation is suppressed in these cases; nevertheless, dynamical evolution still leads to the formation of a sort of bar. A comparison between the evolution in the cases of high and low L suggests that a dynamical instability occurs at the beginning and manifests itself completely in $\sim$ 20 crossing times. After this time, figure rotation is still present for HL and HL_{bis} while the LL and LL_{bis} systems conserve both their shape and their orientation in space.

Based on Figure 6, the change in shape occurs sooner in the case of low angular momentum; for models LL and LL_{bis}, the "stable" phase begins at $\sim 8t_{cross}$ in the luminous component and at $\sim 18t_{cross}$ in the dark component. In addition, in the absence of rotation, the final elongation in the dark matter is greater: $0.64 < b/a < 0.69$ and $0.6 < c/a < 0.67$. Rotational motion has the effect of breaking slightly the axisymmetry reached by the model.

This evolution is strongly reminiscent of the well-known ROI seen in radially-anisotropic, spherical models (Merritt 1999). In spherical models, the instability causes a bar to form with some random orientation, determined by the precise spectrum of density inhomogeneities in the initial model. In the triaxial case, the initial conditions are already bar-like, but the instability chooses a new bar-like distortion to grow. As in the spherical case, the final configuration after the instability has run its course is close to prolate.

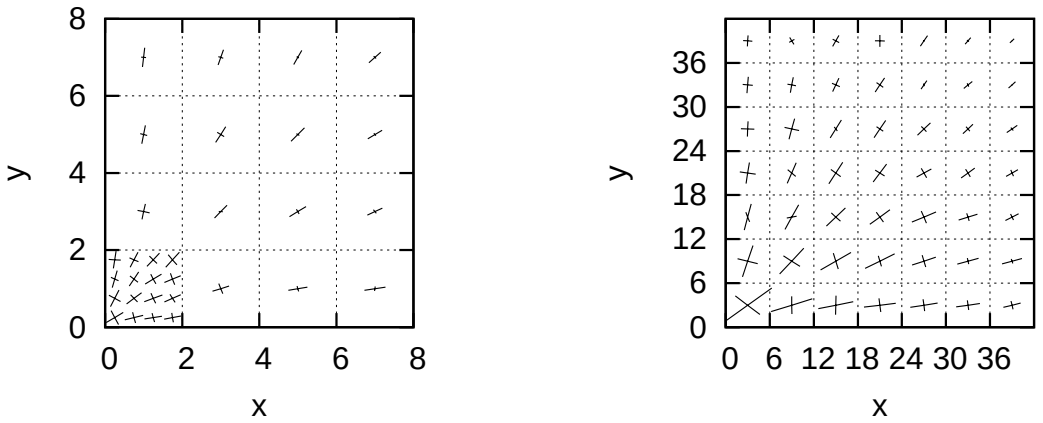

FIG. 4.— Velocity dispersions of $MOD1-bis$ in the case of luminous matter (left) and for the dark matter (right). The components of the velocity dispersions were stored in each cell of a grid divided as described in the text. The length of the arms of each cross is proportional to the corresponding principal dispersion.

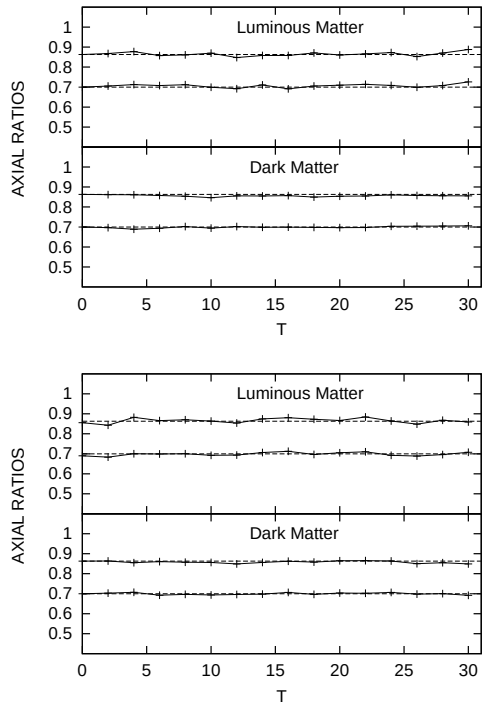

FIG. 5.— Upper panels: evolution of the axis ratios for the solution MOD1-bis in the fixed-potential integrations. Lower panels: evolution of the axis ratios for the solution MOD1. The axis ratios are evaluated at $r = 8$ for the luminous matter and at $r = 25$ for the dark component. The times are scaled to the internal crossing time.

6. DEPENDENCE OF THE INSTABILITY ON THE ORBITAL COMPOSITION

In spherical models, the ROI is associated with a predominance of eccentric orbits. The instability growth rate can be reduced to zero by changing the orbital composition toward more isotropic or tangentially-biased solutions; this is always possible since there are many distribution functions $f(E, J)$ that correspond to the same density profile $\rho(r)$. Likewise, in the triaxial geometry, the Schwarzschild method can yield a variety of orbital solutions consistent with a specified mass model, and these different solutions will generally have different stability properties. Here we show that the instability described above in the triaxial models can indeed be effectively suppressed by reducing the number of semi-radial (box) orbits in the self-consistent solutions. This result reinforces our hypothesis that the instability is intrinsically similar in character to the ROI, and is also of physical significance for real galaxies, as discussed in §7.

6.1. *Minimizing the contribution from semi-radial orbits*

To investigate the hypothesis of ROI, new orbital solutions constraining the number of semi-radial orbits were constructed, discretized and evolved forward in time as N-body systems.

Following Poon & Merritt (2004), the relative contributions of different orbits to the self-consistent solutions was varied by adding a penalty function to equations (1) and (2), which became

$$\chi^2_{lum} = \frac{1}{N_{cells}} \sum_{j=1}^{N_{cells}} \left(M_{j;lm} - \sum_{k=1}^{n_{orb}} C_{k;lm} B_{k,j;lm} \right)^2 + \\ + \sum_{k=1}^{n_{orb}} C_{k;lm} W_{k;lm} \qquad (19)$$

and

$$\chi^2_{dm} = \frac{1}{N_{cells}} \sum_{j=1}^{N_{cells}} \left(M_{j;dm} - \sum_{k=1}^{n_{orb}} C_{k;dm} B_{k,j;dm} \right)^2 + \\ + \sum_{k=1}^{n_{orb}} C_{k;dm} W_{k;dm} \quad , \qquad (20)$$

respectively. Here, $W_{k;lm(dm)}$ is a penalty associated with the kth orbit of the luminous (dark) component; as $W_{k;lm(dm)}$ increases, the mass contribution $C_{k;lm(dm)}$ of the kth orbit in the model decreases. (We remark that the role of our penalty function is that of an *ad hoc* numerical device and does not have any particular physical

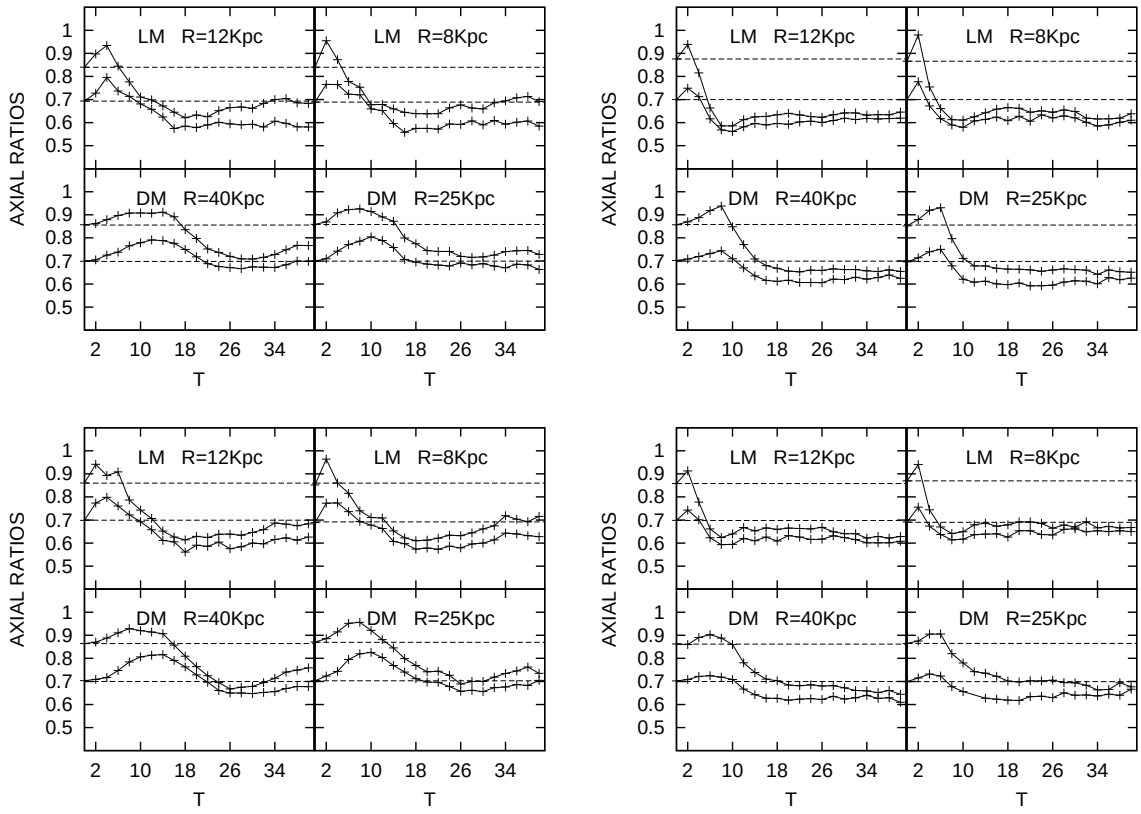

FIG. 6.— Evolution of the axial ratios of HL (top left), LL (top right), HL_{bis} (bottom left) and LL_{bis} (bottom right). R is the distance from the center where the axial ratios are evaluated. The times are scaled to the crossing time.

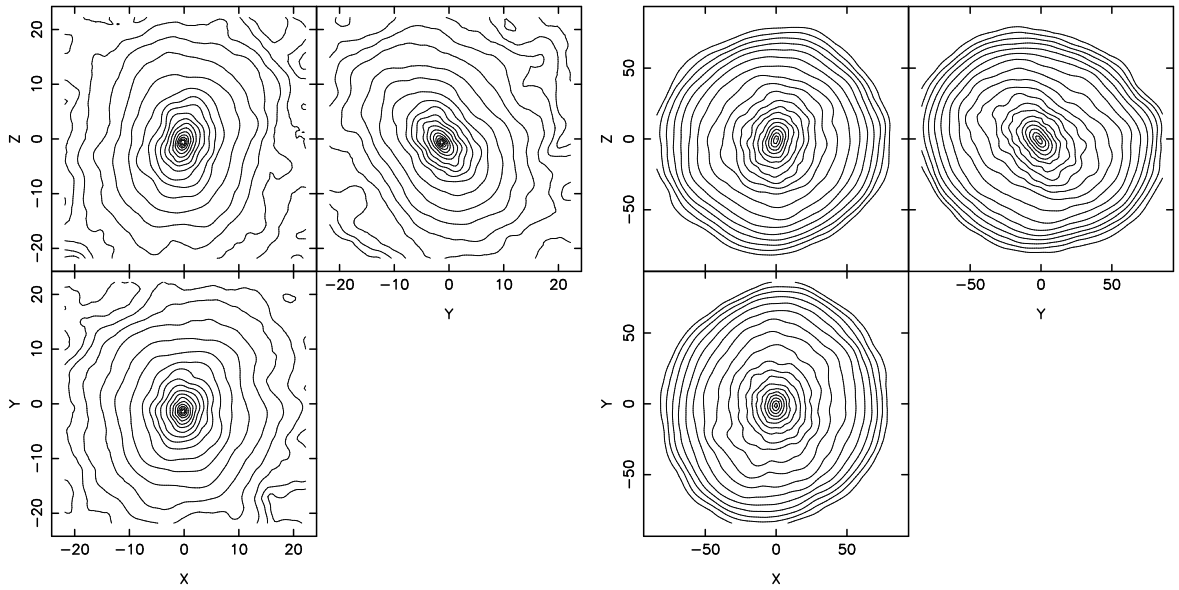

FIG. 7.— Contours of the projected density after 40 crossing times for model HL. Left panels: luminous component; right panels: dark matter component.

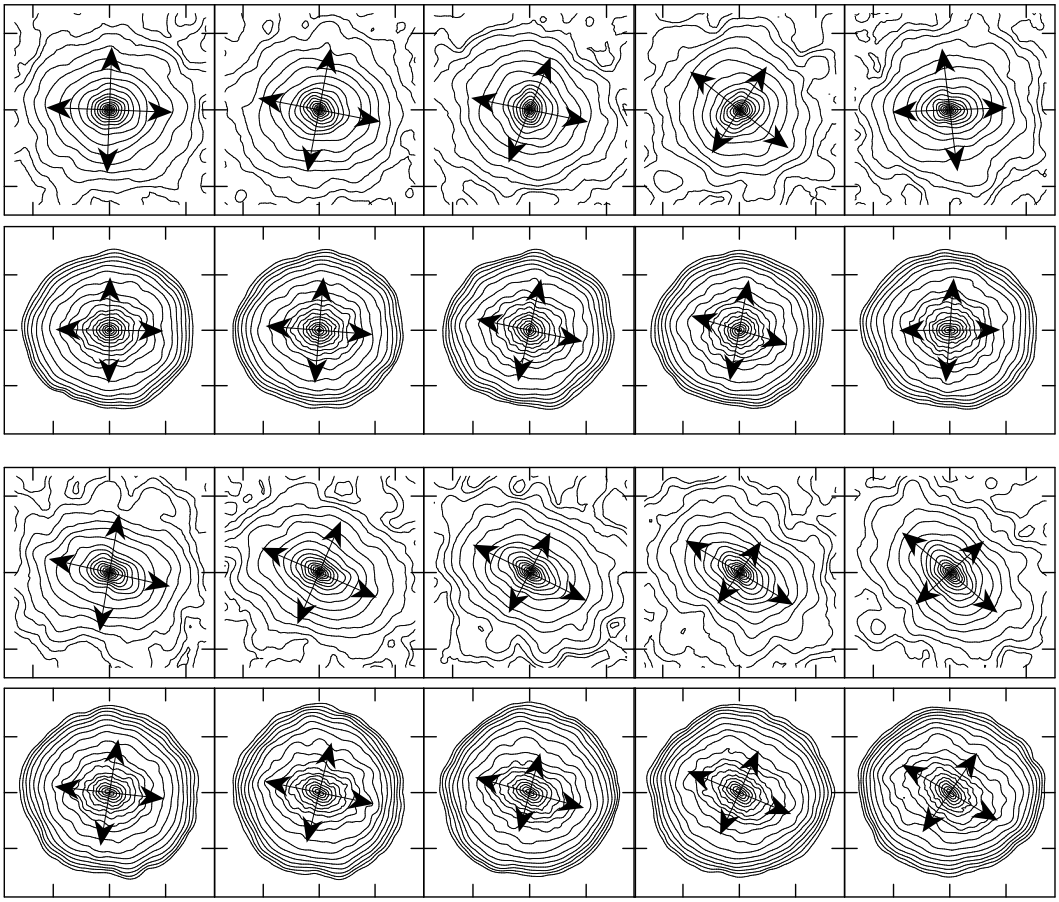

FIG. 8.— Evolution of the isodensity contours in the $y-z$ plane for the model HL_{bis}; the two horizontal set of panels on the top display the configuration at $0, 4, 8, 12, 16t_{cross}$, then, the two bottom set of panels refer to $20, 24, 28, 32, 36t_{cross}$ At each time, the upper panels represent the luminous component while the dark matter is shown into the lower panels. In the case of the luminous matter the linear size of each box is 22 while for the dark matter it is 85. The arrows represent the eigenvectors of the inertia tensor with the highest value of the projection on the $y-z$ plane (in most of the plots, the other eigenvector is approximately along the line of sight). The rotation can clearly be seen after 20 crossing times; by this time the instability appears to have run its course.

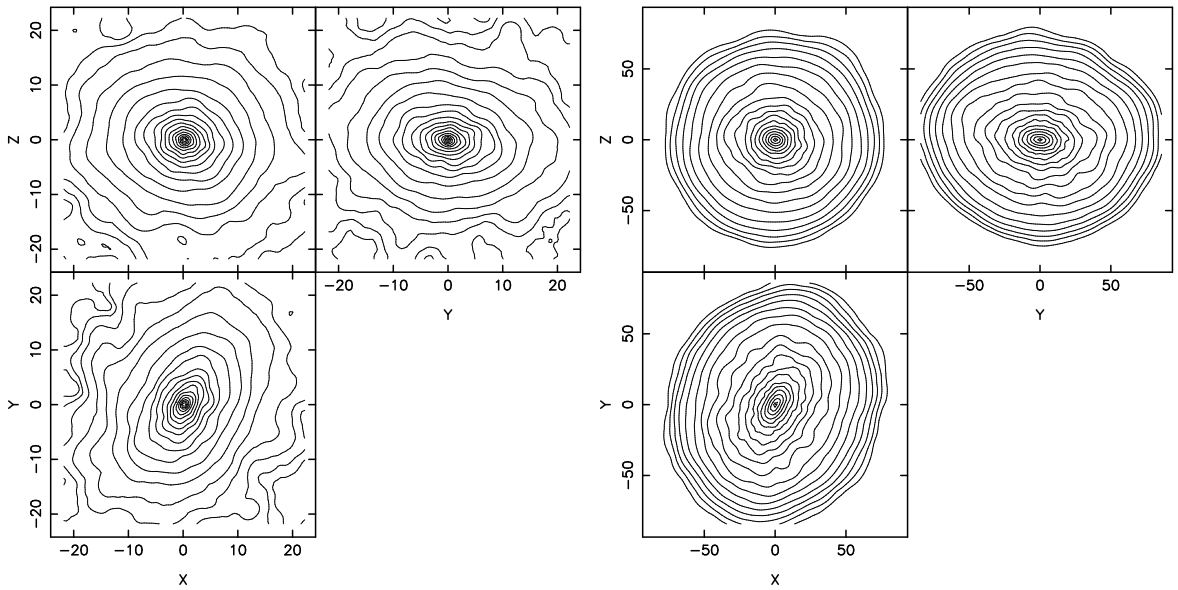

FIG. 9.— Contours of the projected density at 40 crossing times for model LL. Left panels: luminous component; right panels: dark matter component.

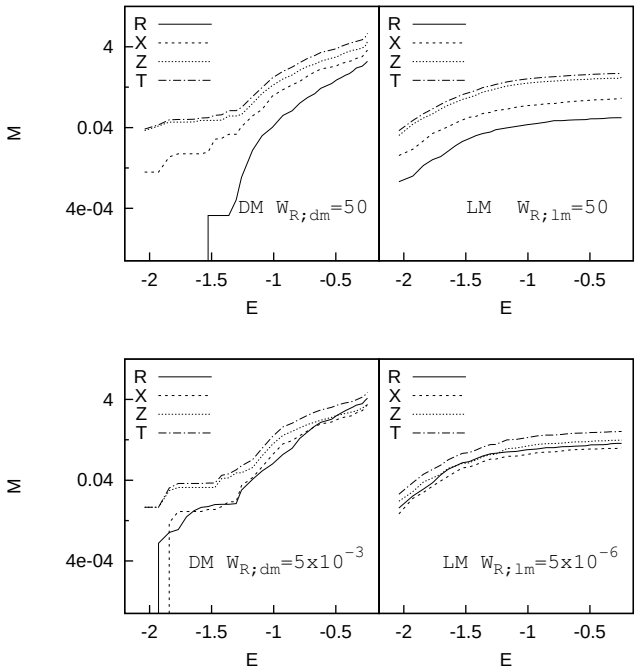

FIG. 10.— Cumulative energy distributions (by mass) of the various orbital families for different values of W_R. The symbols R, X, Z and T denote semi-radial, X-tube, Z-tube and all tube orbits, respectively.

meaning.) We chose $W_{k;lm} = W_{k;dm} = 0$ for the tube orbits and $W_{k;lm} \equiv W_{R;lm} > 0$ and $W_{k;dm} \equiv W_{R;dm} > 0$ for the semi-radial orbits. The optimization problem represented by equations (19) and (20) was solved using the NAG routine E04NCF, which implements an efficient method to solve solves linearly constrained linear least-squares problems and convex quadratic programming problems (Stoer 1971; Gill 1984). The new solutions were found using the full orbital library corresponding to model MOD1-bis.

As shown in Figure 10, setting both $W_{R;dm}, W_{R;lm} > 0$ does in fact increase the number of tube orbits in the solutions at the expense of the semi-radial orbits. The error in the cell masses increases at increasing W_R, as shown in Figure 11. However, it is well known that (e.g. Merritt & Fridman 1996), the value of δ alone is not able to judge the degree of self-consistency of an orbital solution. Therefore, our new solutions might still represent reasonable equilibria even if the quality of the fit to the cell masses is worse than that of the solutions found in CLMV07. We return to this point below.

6.2. *Discretized models and their kinematical properties*

We examined the properties of discretized models for four choices of the penalty parameters:

(i) $W_{R;dm} = W_{R;lm} = 50$ (model $N1$);

(ii) $W_{R;dm} = W_{R;lm} = 5$ (model $N2$);

(iii $W_{R;dm} = 5 \times 10^{-3}$ and $W_{R;lm} = 5 \times 10^{-6}$ (model $N3$);

(iv) $W_{R;dm} = 50$ and $W_{R;lm} = 5 \times 10^{-6}$ (model $N4$).

N-body realizations were generated as explained in §3; the sense of circulation of the tube orbits was chosen randomly. Each model used 2×10^4 luminous particles and 1.5×10^5 dark matter particles. Table 2 gives values

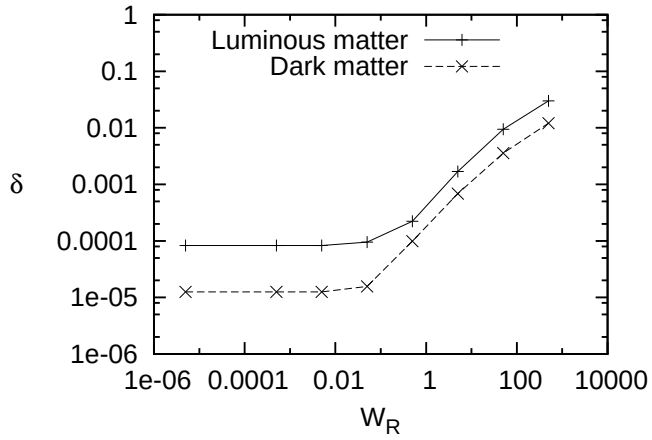

FIG. 11.— Departure from self-consistency (δ) as a function of the "penalty"(W_R).

TABLE 2
ANISOTROPY PARAMETERS OF THE NEW MODELS.

MODEL	$W_{R;lm}$	$W_{R;dm}$	$[2T_r/T_t]_{lm}$	$[2T_r/T_t]_{dm}$
$N1$	50	50	0.512	1.175
$N2$	5	5	0.784	1.335
$N3$	5×10^{-6}	5×10^{-3}	1.220	1.754
$N4$	5×10^{-6}	50	1.230	1.174

of the anisotropy parameters. As expected, $(2T_r/T_t)_{lm}$ and $(2T_r/T_t)_{dm}$ are decreasing functions of W_R.

Figure 12 displays the velocity dispersions of these systems in the $x - y$ plane, clarifying the relation between W_R and the velocity anisotropy: when $W_{R;lm} = 5$ or 50, the tangential velocity dispersion is higher than the radial dispersion in the luminous matter. For $W_{R;lm} = 5 \times 10^{-6}$, we found $\sigma_r \approx \sigma_t$. In the case of the dark component, when $W_{R;dm} = 5$ or 50 the halo is nearly isotropic; in these systems the principal axes of the velocity ellipsoid tend to lose their radial alignment. In the case $W_{R;dm} = 5 \times 10^{-3}$, the dark matter becomes strongly anisotropic.

6.3. *N-body simulations*

The new N-body systems were evolved for 20 crossing times, approximately the time scale of the instability to grow, as seen before.. Figure 13 shows the evolution of the model axis lengths. Model $N3$ is clearly dynamically unstable, evolving into a prolate configuration. By contrast, for models $N1$, $N2$ and $N4$, the instability was either absent or much suppressed. Figures 14 and 15 show contours of the projected density at $t = 20t_{cross}$ for models $N1$ and $N4$ respectively; in these cases, the final configuration looks very similar to the initial one.

The correlation between bar formation and the value of the radial velocity dispersion is a clear sign that the dynamical instability discussed in §4.2 can be identified with the ROI. Furthermore, the behavior of model $N4$ suggests that the instability disappears when the dark halo is made isotropic, i.e., the instability derives mainly from anisotropy in the dark component.

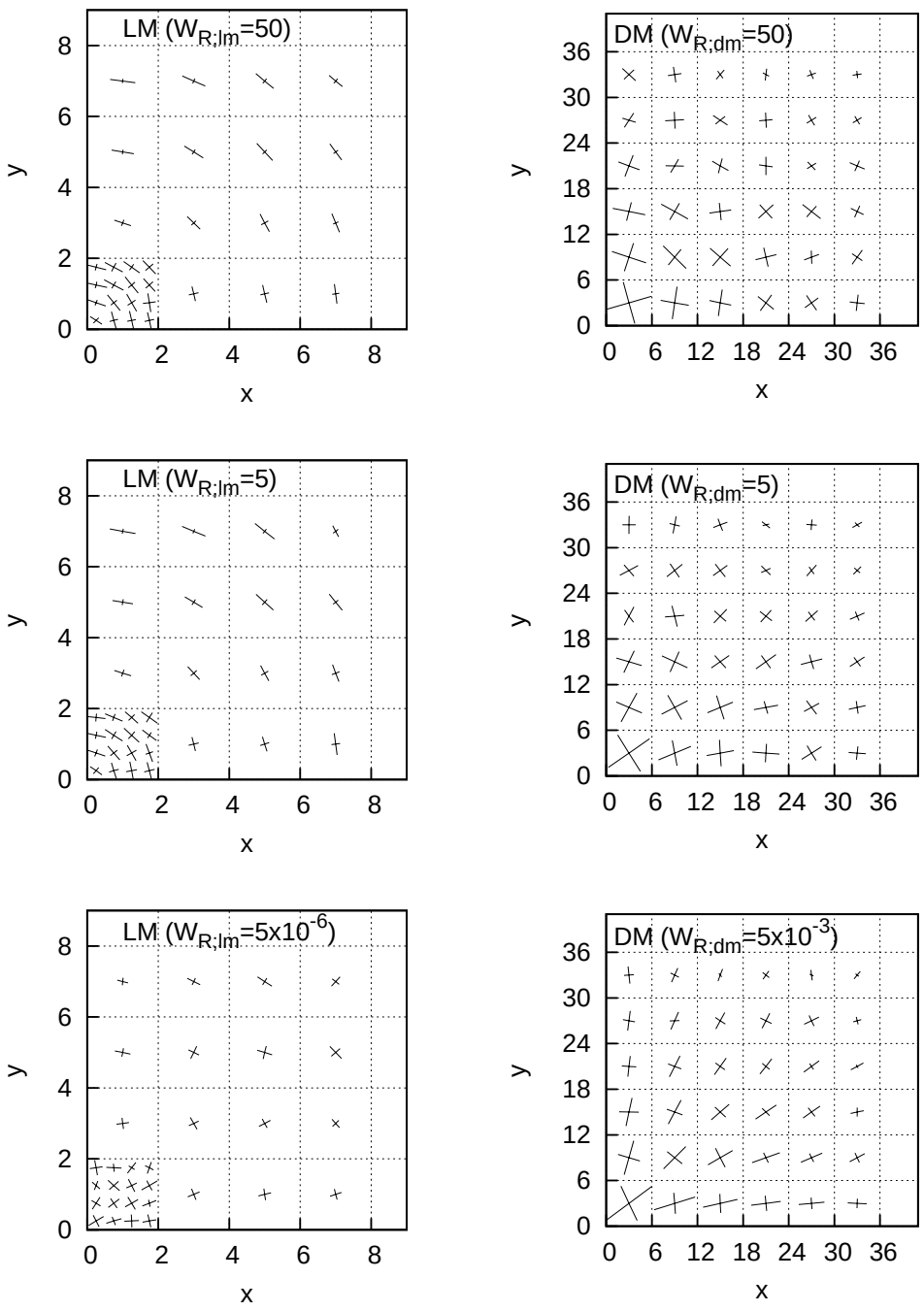

FIG. 12.— Velocity dispersions in model $N1$ ($W_{R,dm} = W_{R,lm} = 50$), $N2$ ($W_{R,dm} = W_{R,lm} = 5$) and $N3$ ($W_{R,dm} 5 \times 10^{-3}$, $W_{R,lm} = 5 \times 10^{-6}$) . The length of the axes of each cross is proportional to the corresponding principal dispersion.

We can draw the following conclusions from these integrations:
1. The dynamical instability disappears when the fraction of semi-radial orbits in the models is decreased.
2. The stability properties of these models are determined primarily by the kinematics of the dark matter halo. In particular, stable configurations are obtained when $(2T_r/T_t)_{dm} \lesssim 1.4$.

7. DISCUSSION

Large-scale simulations of structure formation have shown that dark matter halos, during their evolution, develop universal properties, such as a characteristic density profile, a power-law dependence of phase space density on radius, a linear relation between the velocity anisotropy and the density slope ($\beta - \gamma$ relation), and a particular distribution of shapes and spins (Dubinski & Carlberg 1991; Warren et al. 1992; Navarro et al. 1996; Moore et al. 1999; Taylor & Navarro 2001; Hansen & Moore 2006). Various authors (e.g. Syer & White 1998; Dekel et al. 2003) have argued that dynamical processes during mergers may be responsible for the apparent universality of

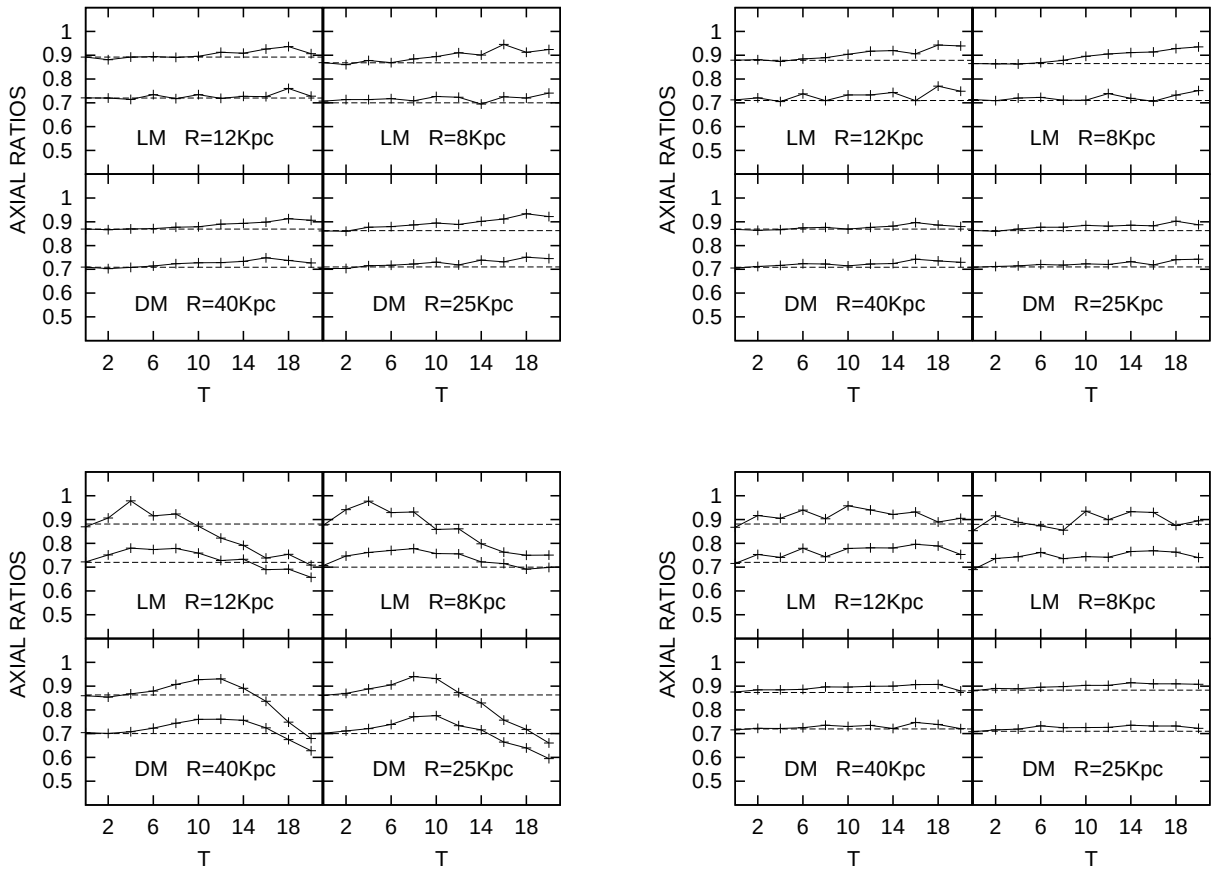

FIG. 13.— Evolution of the axis ratios for new models $N1$ (top left), $N2$ (top right), $N3$ (bottom left) and $N4$ (bottom right). R is the distance from the center where the axial ratios are evaluated. The times are scaled to the crossing time.

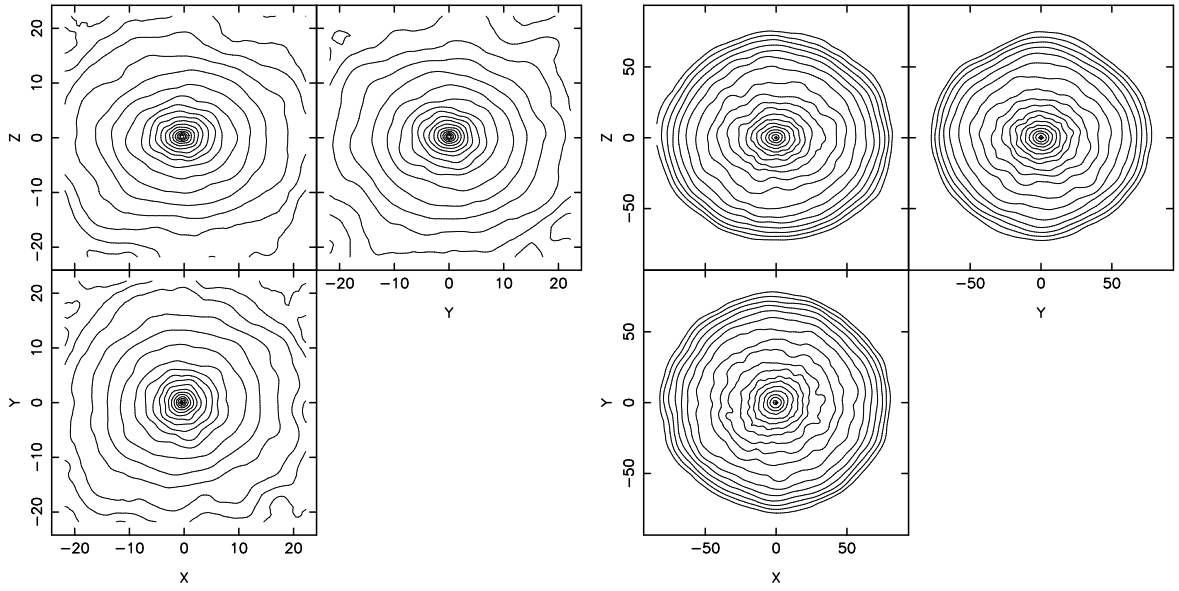

FIG. 14.— Contours of the projected density at 20 crossing times in model $N1$ for both the luminous matter) and the dark matter (right).

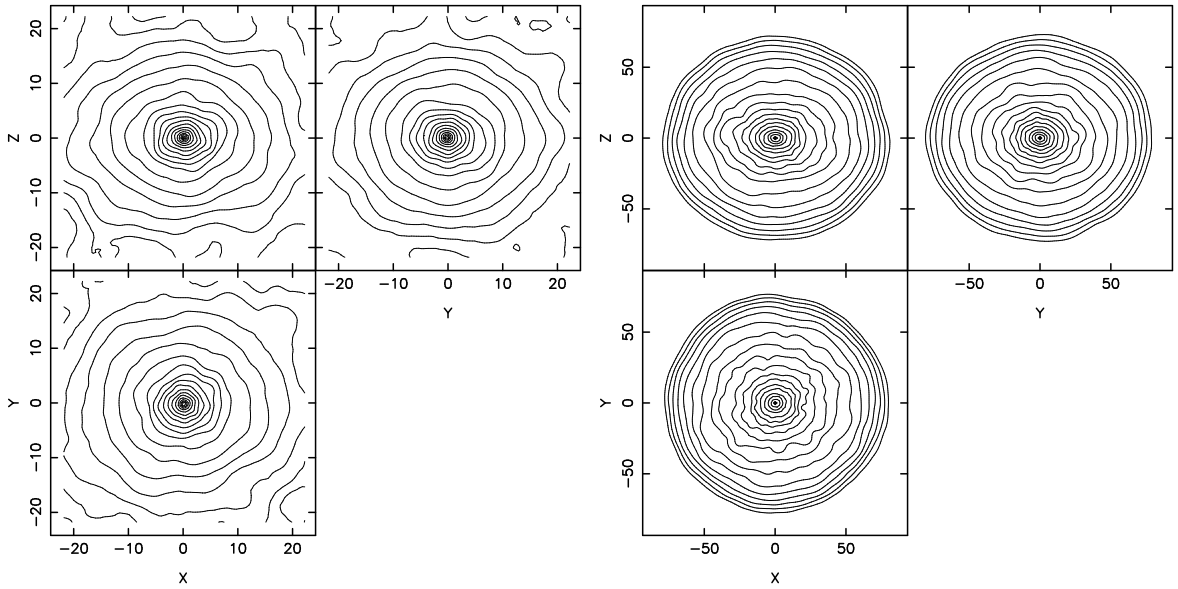

FIG. 15.— Contours of the projected density for the luminous matter (left panels) and the dark matter (right panels) at 20 crossing times in model $N4$.

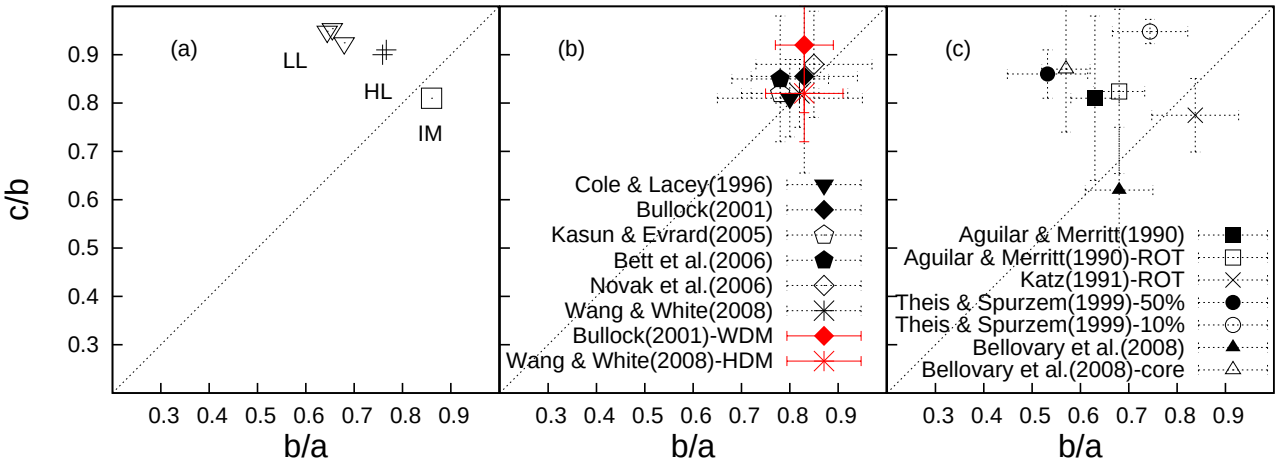

FIG. 16.— *(a)* Axis ratios of the dark matter halos of our evolved unstable models. LL indicates models with low angular momentum while HL refers to rotating models. IM refers to the axial ratios of the initial model. *(b)* Mean axis ratios of dark matter halos in simulations of structure formation in ΛCDM and ΛWDM cosmologies. *(c)* Shapes of equilibrium N-body models formed by isolated cold collapse. Models that were formed from rotating initial conditions are labelled ROT. Theis & Spurzem (1999) give, for a set of 9 dissipationless collapse simulations, the axis ratios of the 50% and 10% of the most bound particles. For Bellovary et al. (2008) we show two values of the final axis ratios of their initially coldest model: one refers to the innermost regions (core) and the other one to a larger distance, roughly the virial radius.

these relations. On the other hand, Huss et al. (1999) and Wang & White (2008) have pointed out that many of these properties are also reproduced in a universe where halos form via monolithic collapse, suggesting that mergers are not essential for establishing the universal relations.

Some of the regularity in dark matter halo properties may be due to dynamical instabilities, which limit the range of allowed equilibrium states irrespective of how the halos formed. A well-established example is the effect of bending instabilities on the shapes of hot stellar systems: major to minor axis ratios are limited to $\sim 3:1$ for both oblate and prolate systems (Merritt & Sellwood 1994). This is a plausible explanation for the lack of elliptical galaxies flatter than Hubble type E7 (Fridman & Polyachenko 1984), and is also consistent with the maximum elongations found for simulated dark matter halos (Bullock 2002; Allgood et al. 2006; Bett et al. 2007).

The role of the ROI in establishing such "universal" characteristics is less clear. The ROI arises naturally in halos formed via monolithic collapse, causing otherwise spherical systems to settle into prolate/triaxial shapes (Merritt & Aguilar 1985; Aguilar & Merritt 1990; Huss et al. 1999). The instability also reduces the dependence of the final concentration on the initial "temperature" of the collapsing cloud (Merritt & Aguilar 1985; Barnes et al. 2005; Bellovary et al. 2008). But formation via mergers is qualitatively different from collapse; and since a (spherical) model can always be rendered stable by making its velocity distribution sufficiently isotropic, the role that the ROI plays in determining the structure of dark matter halos is likely to depend somewhat on the details of the halo formation process.

We nevertheless note that the halos formed in hierarchical cosmologies tend to exhibit radially-anisotropic envelopes, $\sigma_r/\sigma_t \approx 1.5$ (Colín et al. 2000; Wojtak et al. 2005; Navarro et al. 2008), and that these anisotropies are similar to those of unstable models formed via collapse, both before and after the ROI has run its course (Bellovary et al. 2008), and consistent with the values that render our two-component models unstable. So it is plausible that the ROI or something similar is active during the hierarchical formation of halos.

Figure 16 presents a weak test of this idea. Axis ratios of our unstable halo models (panel *a*) are compared with those of dark matter halos formed in various cosmological simulations (panel *b*) and with N-body models formed via simulations of isolated collapse (panel *c*). As noted above, the instability has the effect of making our initially triaxial models more prolate and more elongated. In the absence of rotation (LL), the final shapes are more prolate than for typical cosmological halos. However in the models with streaming motions (HL), the final axis ratios are essentially identical to the average values found in the cosmological simulations. A similar conclusion can be drawn from the isolated collapses in panel (c), which also tend to be more triaxial (i.e. less prolate) when rotation is present.

We stress again that our unstable models could be rendered stable by selecting different sets of orbits, in the same way that unstable spherical models can be stabilized by making their velocity distributions more isotropic. The role of the ROI in structuring dark matter halos must therefore depend somewhat on the orbital composition of halos formed in the cosmological simulations.

8. CONCLUSIONS

We explored the stability properties of two, self-consistent models of triaxial galaxies embedded in triaxial dark matter halos. Our results can be summarized as follows.

1. Both models were found to be dynamically unstable, evolving toward more prolate shapes on a time scale of ~ 20 crossing times. Final shapes were approximately prolate in both components, with short-to-long axis ratios of $\sim 0.6 - 0.7$.

2. The evolution was shown not to be due to errors in construction of the equilibrium models, nor to diffusion of chaotic orbits, but rather to a collective mode. On this basis we identified the instability with the ROI of spherical models.

3. Including streaming motions in the initial models leads to final configurations that are more triaxial than when rotation is absent. These final shapes are very similar to the mean shapes of dark matter halos formed in hierarchical merger simulations.

4. When the number of box-like orbits is reduced below a certain threshold the dynamical instability disappears. The presence or absence of the instability is most strongly affected by the number of box-like orbits in the dark matter halo; stable configurations are obtained when $(2T_r/T_t)_{\rm dm} \lesssim 1.4$.

We thank Linda Leccese, Paolo Miocchi and Alessandro Vicari for helpful discussions. This work was supported by NSF grants AST-0420920 and AST-0807910 and by NASA grant NNX07AH15G.

REFERENCES

Aguilar, L.A., & Merritt, D. 1990, ApJ, 354, 33
Allgood, B., Flores, R. A., Primack, J. R., Kravtsov, A. V., Wechsler, R. H., Faltenbacher, A., & Bullock, J. S. 2006, MNRAS, 367, 1781
Antonov, V. A. 1973, in The Dynamics of Galaxies and Star Clusters, ed. G. B. Omarov (Alma Ata: Nauka), 139
Barnes, E. I., Williams, L. L. R., Babul, A., & Dalcanton, J. J. 2005, ApJ, 634, 775
Bellovary, J. M., Dalcanton, J. J., Babul, A., Quinn, T. R., Maas, R. W., Austin, C. G., Williams, L. L. R., & Barnes, E. I. 2008, arXiv:0806.3434
Bett, P., Eke, V., Frenk, C. S., Jenkins, A., Helly, J., & Navarro, J. 2007, MNRAS, 376, 215
Bullock, J. S. 2002, in The Shapes of Galaxies and Their Dark Matter Halos, Proceedings of the Yale Cosmology Workshop, ed. Priyamvada Natarajan. Singapore: World Scientific, p.109
Burkert, A. 1995, ApJ, 447, L25
Capuzzo-Dolcetta, R., Leccese, L., Merritt, D., & Vicari, A. 2007, ApJ, 666, 165
Cole, S., & Lacey, C. 1996, MNRAS, 281, 716
Colín, P., Klypin, A. A., & Kravtsov, A. V. 2000, ApJ, 539, 561
Dehnen, W. 1993, MNRAS, 265, 250
Dekel, A., Devor, J., & Hetzroni, G. 2003, MNRAS, 341, 326
Dubinski, J., & Carlberg, R.G. 1991, ApJ, 378, 496
Fehlberg, E. 1968, NASA Tech.Rep. TR T-287
Fridman, A. M., & Polyachenko, V. L. 1984, Physics of gravitating systems (Springer)

Gill, P.E. et al. 1984, ACM Trans. Math. Software, 10, 282
Hansen, S. H., & Moore, B. 2006, New Astronomy, 11, 333
Huss, A., Jain, B., & Steinmetz, M. 1999, ApJ, 517, 64
Kasun, S. F., & Evrard, A. E. 2005, ApJ, 629, 781
Katz, N. 1991, ApJ, 368, 325
Kuhlen, M., Diemand, J., & Madau, P. 2007, ApJ, 671, 1135
Lynden-Bell, D. 1979, MNRAS, 187, 101
MacMillan, J. D., Widrow, L. M., & Henriksen, R. 2006, ApJ, 653, 43
Merritt, D. 1980, ApJS, 43, 435
Merritt, D. 1999, PASP, 111, 129
Merritt, D., & Aguilar, L. 1985, MNRAS, 217, 787
Merritt, D., & Sellwood, J. A. 1994, ApJ, 425, 551
Merritt, D., & Fridman, T. 1996, ApJ, 460, 136
Miocchi, P., & Capuzzo-Dolcetta R. 2002, A&A, 382, 758
Moore, B., Ghigna, S., Governato, F., Lake, G., Quinn, T., Stadel, J., & Tozzi, P. 1999, ApJ, 524, L19
Navarro, J. F., Frenk, C. S., & White, S. D. M. 1996, ApJ, 462, 563
Navarro, J. F., Ludlow, A., Springel, V., Wang, J., Vogelsberger, M., White, S. D. M., Jenkins, A., Frenk, C. S., & Helmi, A. 2008, arXiv:0810.1522
Novak, G. S., Cox, T. J., Primack, J. R., Jonsson, P., & Dekel, A. 2006, ApJ, 646, L9
Poon, M. Y., & Merritt, D. 2004, ApJ, 606, 774
Polyachenko, V. L., & Shukhman, I. G. 1977, Soviet Astronomy Lett., 3, 134
Schwarzschild, M. 1979, ApJ, 232, 236
Syer, D., & White, S. D. M. 1998, MNRAS, 293, 337
Smith, B.F., & Miller, R.H. 1982, ApJ, 257, 103
Stoer, J. 1971, SIAM Numer. Anal., 8, 382
Taylor, J. E., & Navarro, J. F. 2001, ApJ, 563, 483
Theis, Ch., & Spurzem, R. 1999, A&A, 341, 361
Toomre, A. 1966, in Geophysical Fluid Dynamics, Notes on the 1966 Summer Study Program at the Woods Hold Oceanographic Institution (Ref. No. 66-46) (Woods Hole: Woods Hole Oceanographic Inst.), 111
Wang, J., & White, S. D. M. 2007, MNRAS, 380, 93
Warren, M. S., Quinn, P. J., Salmon, J. K., & Zurek, W. H. 1992, ApJ, 399, 405
Wojtak, R., Łokas, E. L., Gottlöber, S., & Mamon, G. A. 2005, MNRAS, 361, L1